Mon. Not. R. Astron. Soc. **328,** 112–126 (2001)

X-ray beaming caused by resonance scattering in the accretion column of magnetic cataclysmic variables

Y. Terada,[1★] M. Ishida,[2] K. Makishima,[1] T. Imanari,[3] R. Fujimoto,[4] K. Matsuzaki[4] and H. Kaneda[4]

[1]*Department of Physics and Science, University of Tokyo, 7-3-1, Hongo, Bunkyo-lu, Tokyo, 113-0033 Japan*
[2]*Department of Physics, Tokyo Metropolitan University, 1-1 Minami-Ohsawa, Hachioji-shi, Tokyo, 192-0397 Japan*
[3]*Engineering, The University of Tokyo, 7-3-1, Hongo, Bunkyo-lu, Tokyo, 113-0033 Japan*
[4]*The Institute of Space and Astronautical Science, 3-1-1, Yoshinodai, Sagamihara, 229-8510 Japan*

Accepted 2001 July 18. Received 2001 May 10; in original form 2001 January 21

ABSTRACT

Extremely strong ionized Fe emission lines, with equivalent widths reaching ∼4000 eV, were discovered by *ASCA* from a few Galactic compact objects, including AX J2315−0592, RX J1802.1+1804 and AX J1842.8−0423. These objects are thought to be binary systems containing magnetized white dwarfs (WDs). A possible interpretation of the strong Fe K line is the line-photon collimation in the WD accretion column, as a result of resonance scattering of line photons. The collimation occurs when the accretion column has a flat shape, and the effect is augmented by the vertical velocity gradient, which reduces the resonant trapping of resonant photons along the magnetic field lines. This effect was quantitatively confirmed with Monte Carlo simulations. Furthermore, with *ASCA* observations of the polar V834 Centauri, this collimation effect was clearly detected as a rotational modulation of the equivalent width of the Fe K emission line. The extremely strong emission lines mentioned above can be explained consistently by our interpretation. Combining this effect with other X-ray information, the geometry and plasma parameters in the accretion column were determined.

Key words: radiation mechanisms: thermal – scattering – methods: observational – stars: individual: V834 Cen – white dwarfs – X-rays: stars.

1 INTRODUCTION

A polar (or AM Her type object) is a binary system consisting of a low-mass main-sequence star filling its Roche lobe and a magnetized white dwarf (WD) with a 10^7–10^8 G magnetic field, which is strong enough to lock the WD spin with the orbital motion. Matter spilling over the Roche lobe of the companion star is captured by the magnetic field of the WD and accretes on to its magnetic poles, emitting hard X-rays via optically thin thermal bremsstrahlung.

Extremely strong ionized iron emission lines have been discovered for a few polars through the X-ray observations made by *ASCA*. For example, AX J2315−0592 has a strong ionized Fe K_α line centred at $6.84^{+0.13}_{-0.09}$ keV, the equivalent width (EW) of which reaches 900^{+300}_{-200} eV (Misaki et al. 1996), and RX J1802.1+1804 has a strong Fe K_α line with EW ∼4000 eV (Ishida et al. 1998). To interpret these strong line emissions as thermal plasma emission, the plasma metallicity needs greatly to exceed one solar abundance; by as much as ∼2 for AX J2315−0592 and 3.04 ± 1.47 solar for RX J1802.1+1804. Although WD binaries often exhibit highly ionized Fe K lines, the implied abundances are usually subsolar, such as $0.4^{+0.2}_{-0.1}$ solar for AM Her (Ishida et al. 1997), 0.63 ± 0.08 solar for EX Hya (Fujimoto & Ishida 1997) and ∼0.4 solar for SS Cyg (Done & Osborne 1997). Therefore, we speculate that the unusually high iron abundances of the present two WD binaries result from some mechanisms which enhance the EW of the line, rather than from high metallicities of the mass-donating stars.

We find a common feature in these two object, which may provide a clue to the strong iron K line. AX J2315−0592 exhibits a large orbital modulation in the 0.7–2.3 and 2.3–6.0 keV light curves (87 ± 2 and 57 ± 2 per cent, respectively), but almost no modulation in the 6.0–10.0 keV band. Similarly, RX J1802.1+1804 exhibits a large (∼100 per cent) orbital modulation amplitude below 0.5 keV in *ROSAT* observations (Greiner, Remillard & Motch 1998), but the *ASCA* light curves are extremely flat (Ishida et al. 1998). The lack of hard-band modulation implies that a constant fractional volume of the accretion columns (which extend from optically thin to continuum X-rays) is observed throughout the rotational phase, and hence the

★E-mail: terada@amalthea.phys.s.u-tokyo.ac.jp

inclination of the orbital plane i is rather small. Thus the soft-band modulation must be a result of changes in absorption by the pre-shock accretion flow, indicating that we observe down on to a single pole at the absorption maximum. This in turn requires the magnetic colatitude β to be close to i. In short, these systems are inferred to have $\beta \sim i \sim 0$. In this paper, we describe such a polar as a 'pole-on line emitter' ('POLE').

We have another example of extremely strong iron K line emitter; an X-ray transient source AX J1842−0423, discovered with *ASCA* in 1996 October, on the Galactic plane in the Scutum arm region (Terada et al. 1999, hereafter Paper I). The most outstanding feature of this object revealed by the *ASCA* gas imaging spectrometer (GIS) is the very conspicuous emission line at $6.78^{+0.10}_{-0.13}$ keV, the EW of which is extremely large at 4000^{+1000}_{-500} eV. To explain the EW of this line, a plasma metallicity as high as $3.0^{+4.3}_{-0.9}$ solar abundance would be required. We found no periodicity over the period range from 62.5 ms to a few hours, the latter being a typical orbital period of polars. In view of the thin thermal spectrum and the allowed source size of $10^{8.5}$–$10^{17.7}$ cm, we concluded in Paper I that AX J1842−0423 is likely to be another POLE, such as AX J2315−0592 or RX J1802.1+1804.

The face-value metallicities of the three objects are so high that we regard these values to be unrealistic. Instead, we consider that the iron K line EW is much enhanced by some mechanism, which may be common to the POLEs. To account for the strong iron K line of three POLEs, the mechanism must account for line enhancement by a factor of 3 or more. In this paper, we develop the possible explanation invoking resonance scattering (Section 2), which has been proposed briefly in Paper I. In the present paper, we carry out Monte Carlo simulations (Section 3) to confirm the proposed mechanism, and verify the effect through *ASCA* observations of the polar V834 Cen (Section 4).

2 LINE ENHANCEMENT AS A RESULT OF RESONANCE PHOTON BEAMING

2.1 Geometrical beaming of Fe resonance line

In a polar system, a flow of matter accreting on to each magnetic pole of the WD is highly supersonic, so that a standing shock is formed close to the WD. The matter is shock-heated up to a temperature k of a few tens of keV (see Appendix A equation A1). The heated plasma cools by radiating bremsstrahlung hard X-ray continuum and line photons, as it flows down the column, to form a hot accretion column of height h and radius r as illustrated in Fig. 1, later. We can assume that the ion temperature is equal to the electron temperature, because the ion to electron energy transfer time-scale $t_{\rm eq}$ is much shorter than the cooling time-scale $t_{\rm ff_{cool}}$ (see Appendix A, equations A7 and A6).

The typical accretion rate of polars is $\dot{M} \sim 10^{16}\,{\rm g\,s^{-1}}$, r is typically 5×10^7 cm, and the velocity immediately beneath the shock front is typically $u^{\rm sh} \sim 10^8\,{\rm cm\,s^{-1}}$ (see Appendix A equation A2), so that the electron density at the top of the hot accretion column is typically $n_e^{\rm sh} \sim 10^{15}$–$10^{16}\,{\rm cm^{-3}}$ (see Appendix A equation A3). The optical depth of the column for Thomson scattering is then given by

$$\tau_{\rm T} = 0.24\left(\frac{r}{5\times10^7\,{\rm cm}}\right)\left(\frac{n_e^{\rm sh}}{7.7\times10^{15}\,{\rm cm^{-3}}}\right), \quad (1)$$

and the optical depth of free–free absorption is much smaller (see Appendix A equation A8). Therefore, the column is optically thin for both electron scattering and free–free absorption, so the continuum X-rays are emitted isotropically.

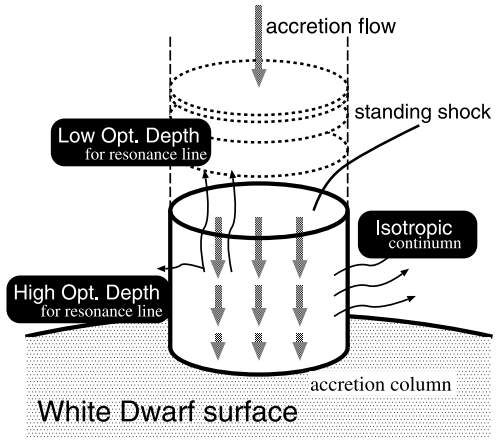

Figure 1. Schematic view of an accretion column on the WD in a polar system.

On the other hand, the optical depth for the resonance scattering is calculated from equation (A10) in Appendix A as

$$\tau_{\rm R} = 36\left(\frac{n_e}{7.7\times10^{15}\,{\rm cm^{-3}}}\right)\left(\frac{A_{\rm Fe}}{4.68\times10^{-5}}\right)\left(\frac{r}{5\times10^7\,{\rm cm}}\right), \quad (2)$$

at the energy of the hydrogenic iron K_α line, where $A_{\rm Fe}$ is the abundance of iron by number, which is normalized to the value of one solar. Thus, the accretion column is optically thick for resonance lines, and the resonance line photons can only escape from positions close to the surface of accretion column. If the accretion column has a flat coin-shaped geometry, and our line of sight is nearly pole-on to it, we will observe the enhanced Fe K lines. We call this effect 'geometrical beaming'. However, this effect can explain the Fe K line enhancement up to a factor of 2.0 (see Appendix B), which is insufficient to explain the enhancements of a factor of ∼3 observed in POLEs. An additional mechanism is clearly needed.

2.2 Additional collimation by vertical velocity gradient

In the accretion column of a polar, both temperature kT and u decrease, and n_e increases from the shock-front towards the WD surface. Numerically, the vertical profiles of these quantities are calculated by Hoshi (1973) and later by Aizu (1973), as a function of vertical distance z from the WD surface, as equation (A4) in Appendix A. Because of the Doppler shift caused by this strong vertical velocity gradient in the post-shock flow, the resonance line energy changes continuously in the vertical direction. Let us consider, for example, that a line photon of rest-frame energy E_0 is produced near the bottom of an accretion column, $z \simeq 0.1h$, where the emissivity of He-like iron line photons reaches its maximum, and that this photon moves vertically by its mean free path of resonance scattering $l_{\rm R}$ which is given as

$$l_{\rm R} = (\sigma_{\rm R} A_{\rm Fe} n_e)^{-1}$$

$$= 1.3\times10^6\left(\frac{z}{h}\right)^{\frac{2}{5}}\left(\frac{n_e^{\rm sh}}{7.7\times10^{15}\,{\rm cm}}\right)^{-1}\left(\frac{A_{\rm Fe}}{4.68\times10^{-5}}\right){\rm cm}. \quad (3)$$

Because h is given as equation (A5) (Appendix A), $l_{\rm R}$ is roughly equal to $0.07h(z/h)^{2/5}$. Over this distance along the z-direction, u will change by $\Delta u = 4.0\times10^6\,{\rm cm\,s^{-1}}$ at $z \simeq 0.1h$, from

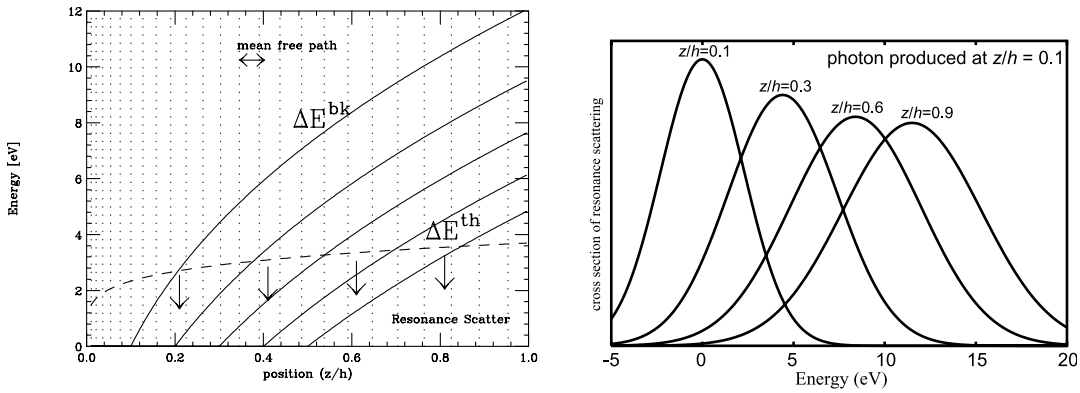

Figure 2. Left-hand panel: the cumulative shift of the resonance energy (solid line) for upward-moving Fe K line photons, which are produced at $z = 0.1h$, $0.2h$, $0.3h$, $0.4h$ and $0.5h$. The thermal width of the resonant Fe K line is given by the dashed curve. The separations of the adjacent dotted vertical lines specify the mean free path $l_{\rm R}$ of resonant photons. Right-hand panel: cross-section of resonance scattering for an iron K_α line photon, which is produced at $z/h = 0.10$ and moves vertically. The resonance centroid energy corresponds to $\Delta E^{\rm bk}$ shown in the left-hand panel, and the resonance energy width corresponds to $\Delta E^{\rm th}$.

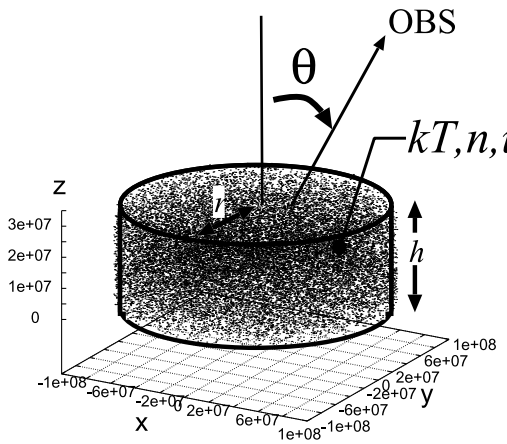

Figure 3. Definition of the cylinder in our simulation.

equation (A4), so the resonance energy for the line photon shifts, caused by the Doppler effect over the same distance, by

$$\Delta E^{\rm bk} = E_0 \frac{\Delta u}{c} = 0.9 \left(\frac{E_0}{6.695\,{\rm keV}}\right)\left(\frac{u^{\rm sh}}{0.9\times10^8\,{\rm cm}^{-3}}\right){\rm eV}, \qquad (4)$$

where c is the light velocity. Fig. 2 shows the change of $\Delta E^{\rm bk}$ for upward-moving photons produced at various depths of the accretion column.

The width ΔE of the resonance scattering (see Appendix A equation A9) is determined by the natural width of the line photon ($\sim$1 eV for an iron K ion) and by the thermal Doppler broadening $\Delta E^{\rm th}$. Because the thermal velocity of ion of mass $m_{\rm i}$ reaches

$$v_{\rm i} = \sqrt{\frac{kT^{\rm sh}}{m_{\rm i}}} = 2.4\times10^7 \left(\frac{z}{h}\right)^{\frac{1}{5}}\left(\frac{m_{\rm i}}{56m_{\rm H}}\right)^{-\frac{1}{2}}\left(\frac{kT^{\rm sh}}{16\,{\rm keV}}\right)^{\frac{1}{2}}{\rm cms}^{-1}, \qquad (5)$$

with $m_{\rm H}$ as the mass of a hydrogen atom, the thermal Doppler width of the resonance becomes

$$\Delta E^{\rm th}(z) = E_0\left(\frac{v_{\rm i}}{c}\right) = 3.7\left(\frac{z}{h}\right)^{\frac{1}{5}}\left(\frac{m_{\rm i}}{56m_{\rm H}}\right)^{-\frac{1}{2}} \times \left(\frac{E_0}{6.695\,{\rm keV}}\right)\left(\frac{kT^{\rm sh}}{16\,{\rm keV}}\right)^{\frac{1}{2}}{\rm eV}. \qquad (6)$$

Here we normalized the equation to the iron atom, $m_{\rm i} = 56m_{\rm H}$. The dashed line in Fig. 2 shows the position dependence of $\Delta E^{\rm th}$, below which the resonance scattering does occur.

Fig. 2 clearly shows that, if a line photon gradually moves upward through repeated scattering, its energy becomes different from the local resonance energy by an amount $\Delta E^{\rm bk}$ (equation 4), which eventually becomes larger than the thermal width $\Delta E^{\rm th}$ (equation 6). Numerically, this ratio for a photon produced at $z = z_0$ can be described as

$$\frac{\Delta E^{\rm bk}(z)}{\Delta E^{\rm th}(z)} = \frac{\Delta u}{v_{\rm i}} = \frac{u^{\rm sh}\left[(z/h)^{\frac{2}{5}} - (z_0/h)^{\frac{2}{5}}\right]}{\sqrt{3\dfrac{\mu m_{\rm H}}{m_{\rm i}}u^{\rm sh}}\left(\dfrac{z}{h}\right)^{\frac{1}{5}}}$$

$$= 5.5\left(\frac{m_{\rm i}}{56m_{\rm H}}\right)^{\frac{1}{2}}\left(\frac{\mu}{0.615}\right)\left[\left(\frac{z}{h}\right)^{\frac{1}{5}} - \left(\frac{z_0}{h}\right)^{\frac{2}{5}}\left(\frac{z}{h}\right)^{-\frac{1}{5}}\right] \qquad (7)$$

$$\simeq 2.2\left(\frac{m_{\rm i}}{56m_{\rm H}}\right)^{\frac{1}{2}}\left(\frac{\mu}{0.615}\right)\left(\frac{\delta z}{h}\right)\left(\frac{z}{h}\right)^{-\frac{4}{5}} (\delta z \ll h), \qquad (8)$$

where $\delta z = z - z_0$, and μ is the mean molecular weight ($\mu = 0.615$ for a plasma of one-solar abundance), and we used the relation of $kT^{\rm sh} = 3\mu m_{\rm H}(u^{\rm sh})^2$ from equations (A1) and (A2). Then, the photon is no longer scattered efficiently, and can escape out. This effect does not occur in the horizontal direction because there is only a little velocity gradient. As a result, a resonant line photon produced near the bottom of the accretion column escapes with a higher probability when its net displacement as a result of random walk is directed upward, rather than horizontally. In other words, iron K line photons are collimated to the vertical direction. We call this effect 'velocity gradient beaming'. The essence of this effect is that the mass of iron, $m_{\rm i}$ in equation (7), is heavy enough for the bulk velocity gradient to overcome the thermal line broadening.

3 MONTE CARLO SIMULATION

The collimation effect described in Section 2 involves significant scattering processes, which make analytic calculation difficult. In this section, we accordingly examine the proposed effect using Monte Carlo simulations.

3.1 Overview of the simulation

Consider a simple cylinder of height h and radius r, filled with

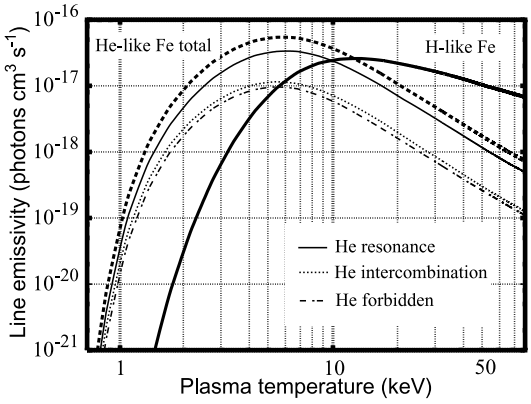

Figure 4. Temperature-dependence of the Fe line emissivity (Mewe et al. 1985) adopted in the calculation.

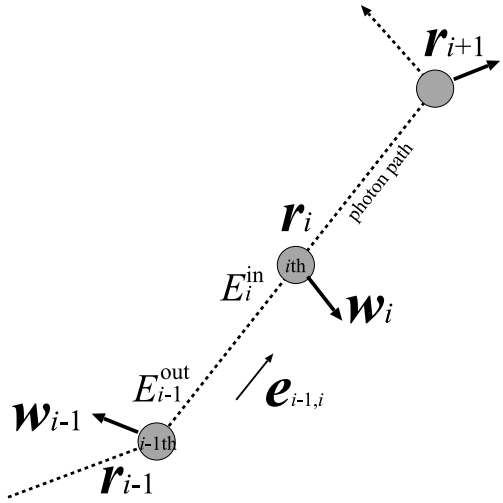

Figure 5. Schematic illustration of each step in our calculation; $\boldsymbol{r}_i$ is the calculation site of the ith step, $\boldsymbol{w}_i$ is the ion motion in the observer's frame, which is a sum of bulk flow motion and random thermal motion, and E_i is the photon energy in the rest frame of ith ion (See text).

X-ray emitting plasma as shown in Fig. 3. We describe the vertical dependence of kT, n_e and u in the cylinder by equation (A4). We then produce a number of Monte Carlo iron line photons in proportion to its emissivity, which in turn is determined by kT and n_e. We isotropically randomize the initial direction of propagation of the iron line photons in the rest frame of iron nuclei. The line energy of each iron photon is also randomized; i.e. the average value of the energy is Doppler-shifted in the frame of observers according to the bulk velocity law (equation 4), and its dispersion is determined by the local thermal motion (equation 5). We trace the propagation of each line photon with a constant step length, which is taken to be 1/100 of the mean free path of resonance scattering at the bottom of the cylinder, where the temperature falls below 1 keV. At each step, the behaviour of the photon is determined by the calculated probabilities of resonance scattering and Compton scattering. We follow the propagation of each photon until it moves outside the cylinder.

3.2 Basic condition

The temperature-dependence of iron line emissivity in optically thin plasma has been calculated by many authors, and we here adopt the calculation by Mewe, Gronenschild & van den Oord (1985) as shown in Fig. 4. We consider four species of iron K line photons; those of an H-like resonance K_α line (6.965 keV), an He-like resonance K_α line (6.698 keV), an He-like intercombination line (6.673 keV), and an He-like forbidden line (6.634 keV). The emissivity of iron line photons per unit volume, in erg s^{-1} cm^{-3}, is described for each species as

$$P = P'(kT) n_{\rm e} n_{\rm Fe}, \tag{9}$$

where $P'(kT)$ in erg s^{-1} cm^{-3} is the value shown in Fig. 4. The iron density $n_{\rm Fe}$, in cm^{-3}, is calculated assuming one solar abundance. The position dependence of iron line emissivity is determined, through equation (9), by the z-dependence of kT and $n_{\rm Fe}$ (equation A4) as shown in Fig. 16 (later).

Treatment of the resonance scattering process, taking into account both the bulk flow and the thermal motion of ions, is a key point of the present simulation. For each line photon being traced, its scattering probability at the ith step $\boldsymbol{r}_i$ is calculated as $\propto n_{\rm Fe}(\boldsymbol{r}_i)\sigma_{\rm RS}(E_i^{\rm in})$, where $n_{\rm Fe}(\boldsymbol{r}_i)$ is the local Fe-ion density at the position $\boldsymbol{r}_i$ (see Appendix A equations A3 and A4), $\sigma_{\rm RS}$ is the cross-section for the resonance scattering given by equation (A9) in Appendix A, and $E_i^{\rm in}$ is the Doppler-shifted energy of the incoming photon measured in the rest frame of a representative Fe-ion at $\boldsymbol{r}_i$. The velocity $\boldsymbol{w}_i$ of this Fe-ion, relative to the observer, is expressed as a sum of the bulk flow velocity u at $\boldsymbol{r}_i$, and a random thermal velocity v. We specifically calculate this as

$$E_i^{\rm in} = E_{i-1}^{\rm out}[1 + (\boldsymbol{w}_{i-1} - \boldsymbol{w}_i)(\boldsymbol{e}_{i-1,i}/c)], \tag{10}$$

where $\boldsymbol{w}_{i-1}$ is the observer-frame velocity (bulk plus random) of the Fe ion that scattered the line photon last time, $E_{i-1}^{\rm out}$ is the outgoing photon energy as expressed in the rest frame of the previous scatterer and $\boldsymbol{e}_{i-1,i}$ is the unit vector along the photon propagation direction from the $(i-1)$th to the ith scattering site (Fig. 5). If the scattering occurs at $\boldsymbol{r}_i$, we randomize the line photon energy from $E_i^{\rm in}$ to $E_i^{\rm out}$ according to the natural width, and isotropically randomize the direction of the outgoing photon in the rest frame of the present scatterer. If, instead, the scattering does not occur at $\boldsymbol{r}_i$, we proceed to the next step without changing its direction. Thus, our calculation automatically includes both the bulk-flow Doppler effect and the thermal broadening. However, we do not consider energy shifts by the ion recoil, which are completely negligible. The scattering probability for a non-resonant photon is set to 0.

In addition to the resonance scattering, we must consider the Compton scattering process; the energy E is shifted to $E/[1 + (E/m_{\rm e}c^2)(1 - \cos\theta_{\rm CMP})]$, where $\theta_{\rm CMP}$ is the Compton scattering angle. For an iron K_α photon with energy $E \sim 6.8$ keV, a Compton scattering with $\theta_{\rm CMP} \geq 10^\circ$ will change the photon energy beyond the resonance energy width of a few eV: then the resonance scattering can no longer occur after a large-angle Compton scattering. We take this effect into account in our simulation, using the probability distribution of $\theta_{\rm CMP}$ by the Klein–Nishina formula, which is almost identical to the classical formula for the energy of iron lines. The differential scattering cross-section and the energies of scattered photons are calculated in the rest frame of the currently scattering electron, so that the anisotropic effects caused by the bulk motion of electron is also included. Note that we neglect the process where the energy of a Compton-scattered continuum photon comes accidentally into the resonance energy range, as we do not generate continuum photons in the Monte Carlo simulation.

3.3 Results

First we simulated the simplest case wherein the plasma is hydrostatic with a single temperature and a single density: i.e. u is set to 0 and there is no vertical gradient in kT or n_e. The angular distributions of line photon flux, calculated under this simple condition for various densities, are shown in Fig. 6. The results confirm that the photons are emitted isotropically when the plasma density is low, but as the density increases, the geometrical beaming becomes progressively prominent. At $n_e = 10^{16}$–$10^{17}\,\mathrm{cm}^{-3}$, the Monte Carlo result agrees nicely with the analytic solution, which assumes a completely optically thick condition; i.e. line photons emit only from the surface of the accretion column (equation B1; see Appendix B). This verifies the proper performance of our Monte Carlo simulation.

Next we have fully considered the vertical gradient in kT, u, and n_e (equation A4). Fig. 7 shows the calculated angular distribution of an He-like iron line when the relevant parameters are set to the nominal values in equations (A1), (A2) and (A3). The resonance line flux is thus enhanced in the vertical direction more strongly than in Fig. 6. This reconfirms the physical beaming mechanism we proposed in Section 2. It is confirmed that the Compton scattering reduces the collimation only slightly. Finally, the intercombination photons, which are free from the resonance scattering, exhibit a nearly isotropic distribution.

We repeated the Monte Carlo simulations by changing h/r, n^{sh}, kT and u^{sh}, around their baseline values of $kT = 16.0\,\mathrm{keV}$, $u^{\mathrm{sh}} = 0.9\times10^{8}\,\mathrm{cm\,s^{-1}}$, $n_e^{\mathrm{sh}} = 7.7\times10^{15}\,\mathrm{cm^{-3}}$, $r = 5\times10^{7}\,\mathrm{cm}$ and $h = 1.9\times10^{7}\,\mathrm{cm}$ (Appendix A). Fig. 8 summarizes the obtained results in terms of the beaming factor

$$\xi_{\mathrm{m}} \equiv \frac{f(0)}{\int_0^{\frac{\pi}{2}} f(\theta)\,\mathrm{d}\cos\theta}, \tag{11}$$

where $f(\theta)$ is the angular distribution of line photon flux, such as is shown in Fig. 7. The beaming factor ξ_{m} increases as h/r decreases (i.e. coin-shaped column), or density increases (Figs 8a and b). However, when the density exceeds $\sim10^{16}\,\mathrm{cm^{-3}}$, the beaming effect diminishes again, because of large-angle Compton scattering. This inference is achieved by comparing results with and without Compton process (Fig. 8b). The WD mass dependence of ξ_{m} is small (Fig. 9): it increases slightly with mass increases because shock velocity increases with deeper gravity potential, and it starts decreasing because density decreases. These results show clearly that the strong collimation of He-like iron K_α photons, with $\xi_{\mathrm{m}} \geq 2$, is possible under reasonable conditions.

4 AN OBSERVATIONAL APPROACH

In order to verify our interpretation experimentally, it is necessary to measure the equivalent width of the resonant Fe K lines as a function of viewing angle. For that purpose, we may utilize a polar of which our line-of-sight relative to the magnetic axis changes from ~0° (pole-on) to ~90° (side-on), as the WD rotates. Among the polars with well-determined system geometry (via optical, ultraviolet and infrared observations), V834 Cen is particularly suited: its orbital plane is inclined to our line of sight by $i = 45 \pm 9°$, and its magnetic colatitude is $\beta = 25 \pm 5°$ (Cropper 1990). As a result, our line of sight to the accretion column changes from 20° to 70°.

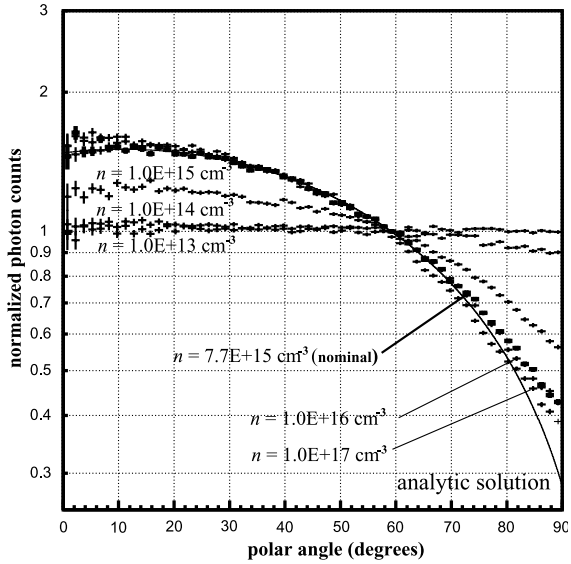

Figure 6. Angular distributions of resonant line photons emergent from a simple thin thermal plasma, simulated by neglecting the vertical motion ($u = 0$) and neglecting the vertical gradient in n and kT. Abscissa is the angle θ defined in Fig. 3, and ordinate is the photon flux per unit steradian normalized to the value of an isotropic emission. The plasma parameters are set to the nominal values; $kT = 16\,\mathrm{keV}$, $r = 5\times10^{7}\,\mathrm{cm}$, and $h = 1.9\times10^{7}\,\mathrm{cm}$. The solid line represents the analytic solution when only the column surface shines (equation B1). The crosses show the calculated results for various densities as given in the figure.

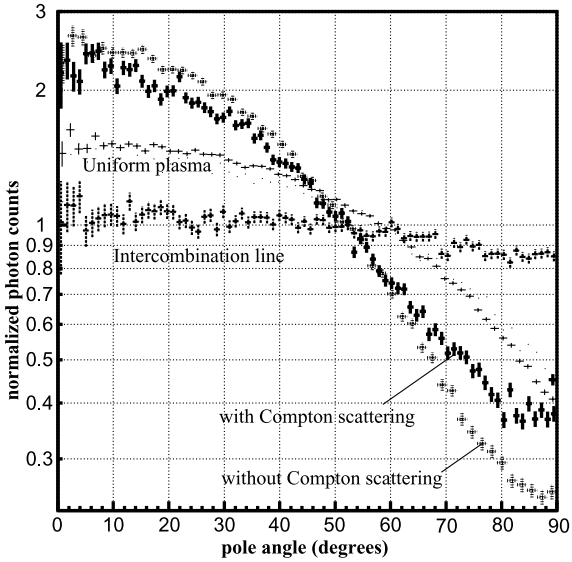

Figure 7. The same as Fig. 6, but calculated for the He-like iron K_α lines while considering the vertical structure of the accretion column. The plasma parameters are set to the nominal values given in Appendix A: $kT^{\mathrm{sh}} = 16\,\mathrm{keV}$, $u^{\mathrm{sh}} = 0.9\times10^{8}\,\mathrm{cm\,s^{-1}}$, $n_e^{\mathrm{sh}} = 7.7\times10^{15}\,\mathrm{cm^{-3}}$, $r = 5\times10^{7}\,\mathrm{cm}$ and $h = 1.9\times10^{7}\,\mathrm{cm}$. Thick solid crosses represent the results when Compton scattering is considered, while dashed crosses represent those neglecting the Compton process. The dotted crosses show the profile of the intercombination line. The thin crosses show the same profile as presented in Fig. 6 (nominal case).

4.1 Observations of V834 Cen with *ASCA*

ASCA has four X-ray telescopes (XRT; Selemitsos et al. 1995), and its common focal plane is equipped with two gas imaging spectrometers (GIS; Makishima et al. 1996; Ohashi et al. 1996) and

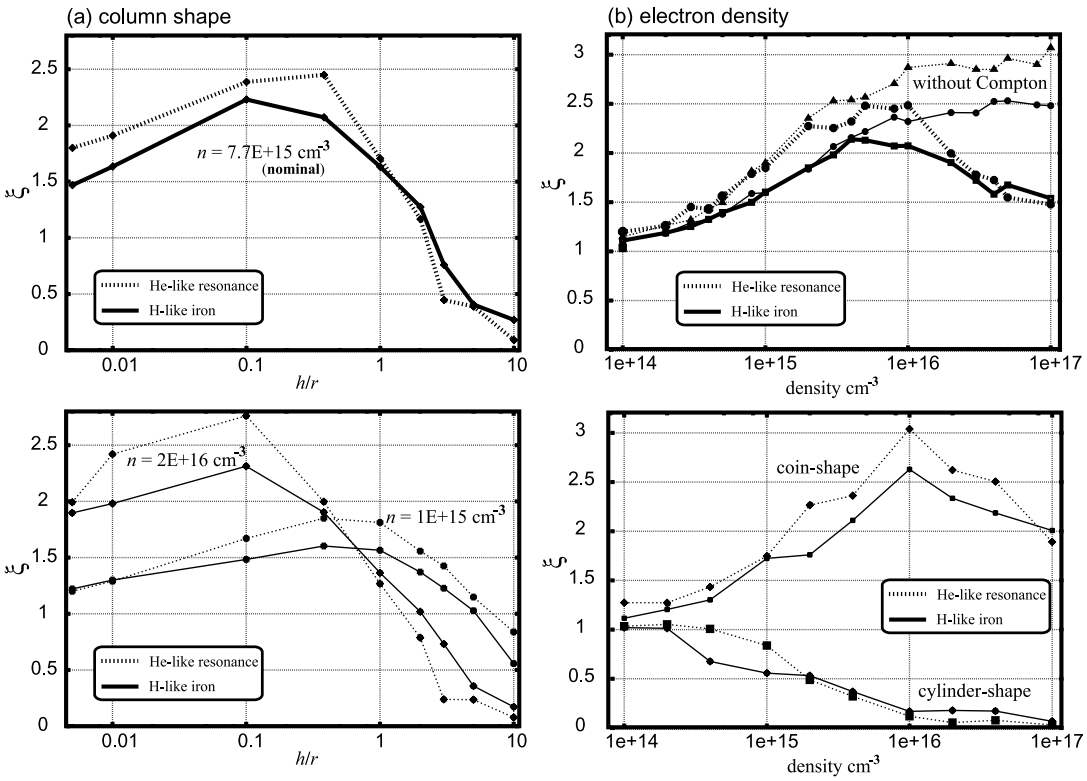

Figure 8. A summary of Monte Carlo simulations. The beaming factor ξ_m is presented for various column shapes and densities. The H-like iron line is represented by solid lines and the He-like iron resonance line by dashed lines. The baseline condition of the calculation is given in the text. Left-hand panels (a): the shape-dependence of ξ_m, where the volume r^2h is fixed. Calculation is performed for three densities as specified in the figure. Right-hand panels (b): the density-dependence of ξ_m for three different column shapes (coin shape, nominal and cylinder shape). The coin-shaped column has $r = 1 \times 10^8$ cm and $h = 1 \times 10^7$ cm, while the cylinder-shaped column has $r = 1 \times 10^7$ cm and $h = 1 \times 10^8$ cm. The beaming factors without Compton scattering are also shown.

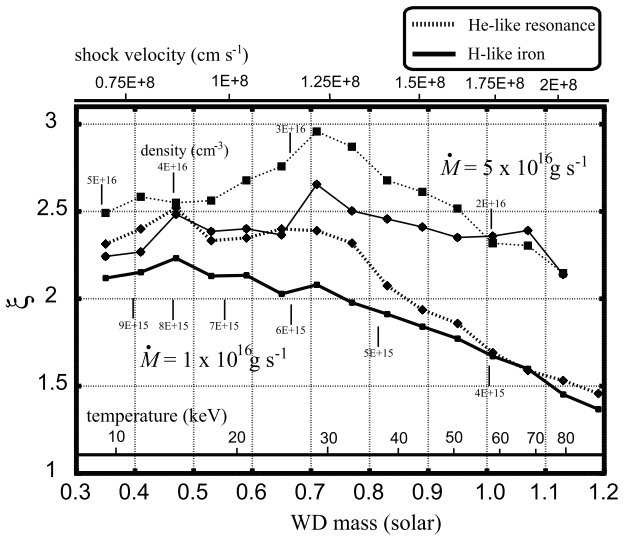

Figure 9. The beaming factor ξ_m with various WD masses. The H-like iron line is represented by solid lines and the He-like iron resonance line by dashed lines. The baseline condition is given in the text, and the temperatures and the densities change with WD mass and WD radius as shown in equations (A1) and (A2). The accretion rate to WD $\dot{M}$ for calculation is set to 1×10^{16} g s and 5×10^{16} g s^{-1}.

two solid-state imaging spectrometers (SIS; Burke et al. 1991; Yamashita et al. 1997). The *ASCA* observation of V834 Cen was carried out for about 20 ks from 1994 March 3.63 to 1994 March 4.13 (UT), and about 60 ks from 1999 February 9.93 to 1999 February 10.72 (UT). In these observations, the GIS was operated in PH-nominal mode, which yields 0.7–10.0 keV X-ray spectra in 1024 channels, and the SIS was operated in 1-CCD FAINT mode, which produces 0.4–10.0 keV spectra in 4096 channels. The target was detected with a mean count rate of 0.171 counts s^{-1} per cent GIS detector and 0.259 counts s^{-1} per cent SIS detector in 1994. The corresponding count rates were 0.191 and 0.253 c s^{-1} in 1999.

For extracting the source photons, we accumulated the GIS and SIS events within a circle of radius 4.5 arcmin, centred on V834 Cen, and employed the following data-selection criteria. We discarded the data during the *ASCA* pass through the South Atlantic Anomaly. We rejected the events acquired when the field of view (FOV) of *ASCA* was within 5° of the Earth's rim. Furthermore, for the SIS we discarded the data acquired when the FOV is within 10° of the bright Earth rim and those acquired near the day–night transition of the spacecraft.

4.2 Light curves

Fig. 10 shows the energy-resolved light curve of V834 Cen obtained with *ASCA* SIS+GIS folded by its rotational period, 1.691 94 hr (Schwope et al. 1993). The phase is coherent between the two light curves. The pole-on phase of V834 Cen is determined by the optical photometry and polarimetry as shown in table 1 of Bailey et al. (1983), which corresponds to a phase $\phi \sim 0.65$–0.85 in our X-ray light curve. We can recognize small dips in light curves of the softer two energy bands in Fig. 10 at $\phi \sim 0.65$ in 1994 and $\sim$0.86 in 1999. These dips are thought to arise from photoelectric absorption by the pre-shock matter on the accretion

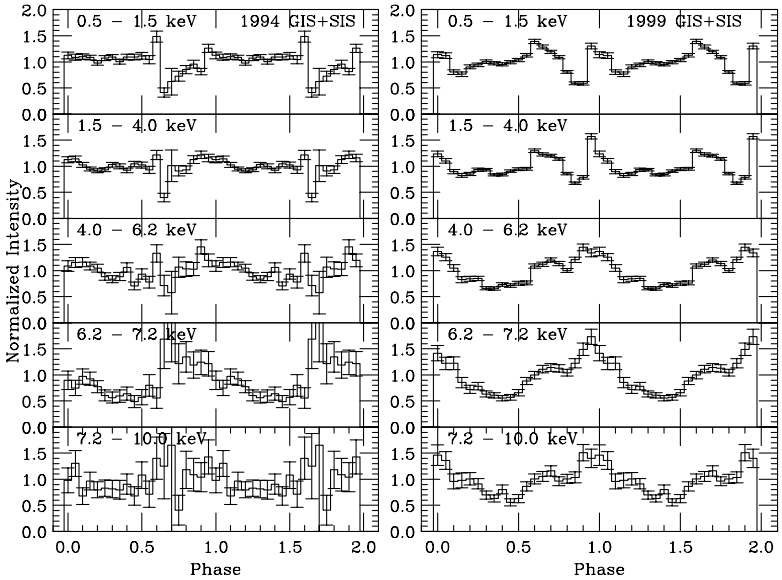

Figure 10. Energy-resolved light curves of V834 Cen obtained with *ASCA*, folded at 1.69 194 hr. Phase $\phi = 0$ corresponds to HJD 244 5048.950 0, which is common to the 1994 and 1999 light curves. Each light curves is shown for two cycles. The left-hand panel shows the observation in 1994, the right-hand panel in 1999.

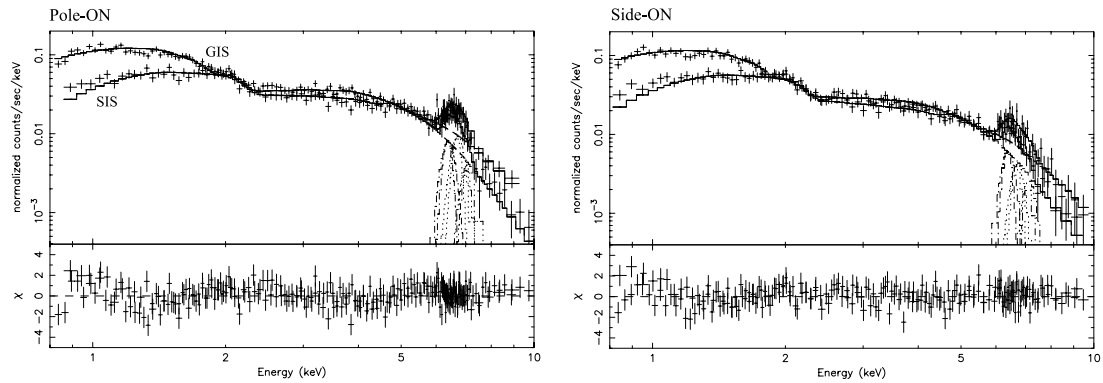

Figure 11. *ASCA* X-ray spectra of V834 Cen taken in 1999, shown without removing the instrumental responses. The left-hand panel shows the spectra in the pole-on phase ($\phi = 0.73 \pm 0.25$), and the right-hand panel shows those in the side-on phase ($\phi = 0.23 \pm 0.25$). The GIS and SIS data are shown with crosses. The solid crosses show the best-fitting model consisting of single temperature bremsstrahlung continuum with partially covered absorption and three narrow Gaussians (see text). The best-fitting parameters are shown in Table 1 Model 4 and in Table 3 (full band fitting). The lower panels show the fit residuals.

column. Therefore, the pole-on phase is consistent between the optical and X-ray data sets. The folded light curve in the iron line energy band (6.2–7.2 keV) exhibits a hump at or near this pole-on phase, suggesting that the proposed line photon enhancement is indeed taking place in this system. However, detailed examination of the modulation of iron line emission needs phase-resolved spectroscopy, performed in the next subsection.

4.3 Spectral analysis

Because the folded light curves (Fig. 10) have different shapes between the two observations, and because the spectral information of GIS-3 in 1994 was degraded by a temporary malfunctioning in the GIS onboard electronics, we use only the 1999 data for spectral analysis. We have accumulated the GIS (GIS2+GIS3) and SIS (SIS0+SIS1) data over the pole-on phase ($\phi = 0.73 \pm 0.25$) and side-on phase ($\phi = 0.23 \pm 0.25$) separately. We subtracted the background spectrum, prepared by using the blank sky data of the GIS and SIS. The spectra, thus derived and shown in Fig. 11, exhibit an absorbed continuum with strong iron K_α emission lines over the 6.0–7.2 keV bandpass.

4.3.1 Continuum spectra

We attempted to quantify the 0.8–10.0 keV continua, neglecting for the moment the line energy band of 6.0–7.2 keV. However, the simplest spectral model for polars, namely a single temperature bremsstrahlung continuum absorbed by one single column density, failed to reproduce either of the observed spectra (Fig. 12 left; Model 1 in Table 1). This failure is not surprising, considering that polars generally exhibit multitemperature hard X-ray emission with complex absorption by the pre-shock absorber (Norton & Watson 1989). The extremely high temperature obtained by this simple fitting, >200 keV, is presumably an artefact, compared with the temperature of 14.7 keV measured with *Ginga*.

To estimate the hottest component of the continuum accurately, avoiding complex absorption in soft energies, we then restricted the fitted energy band to a narrower hard energy band of 4.5–10.0 keV (Model 2 in Table 1). This lower limit (4.5 keV) was determined in a way that is described in section 3.2 of Ezuka & Ishida (1994). In this case, $N_{\rm H}$ is determined solely by the depth of the iron K-edge absorption at ~7.1 keV. This model has been successful on the spectra of both phases, yielding a temperature

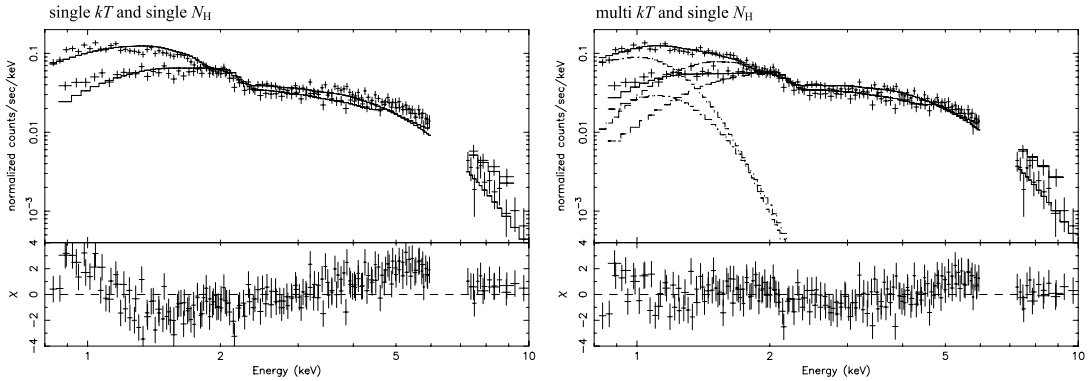

Figure 12. The same spectra as in Fig. 11 left (pole-on). The left-hand panel shows the best-fitting model of single temperature bremsstrahlung absorbed by a single column density. The best-fitting parameters are shown in Table 1 Model 1. The right-hand panel shows the best-fitting model of double temperature bremsstrahlung absorbed by a single column density, corresponding to Model 3 of Table 1 (free kT).

Table 1. Best-fitting continuum parameters for the GIS and SIS spectra of V834 Cen.[a]

Model[b]	kT_1 (keV)	kT_2 (keV)	N_{H1} ($\times10^{22}$ cm^{-2})	N_{H2} ($\times10^{22}$ cm^{-2})	Cov. Frac[c] (per cent)	Bol. lum.[d] (10^{31} erg s^{-1})	χ^2_ν (dof)
POLE-ON phase							
Model 1	>200	–	$0.12^{+0.02}_{-0.02}$	–	–		2.19 (188)
Model 2[e]	$10.8^{+26.8}_{-4.8}$	–	$14.5^{+8.1}_{-8.0}$	–	–	4.99	0.49 (94)
Model 3	>158	$0.19^{+0.01}_{-0.01}$	$0.82^{+0.08}_{-0.08}$	–	–	2.83	1.01 (186)
	14.7[f]	$0.15^{+0.01}_{-0.01}$	$1.21^{+0.08}_{-0.08}$	–	–		1.64 (187)
Model 4	>164	–	<0.02	$7.41^{+2.26}_{-1.70}$	$41.3^{+3.4}_{-3.3}$	3.99	0.91 (186)
	14.7[f]	–	<0.08	$8.83^{+1.90}_{-1.59}$	$60.4^{+2.4}_{-2.5}$		1.00 (187)
SIDE-ON phase							
Model 1	>171	–	<0.04	–	–		1.00 (174)
Model 2[e]	$12.4^{+180}_{-7.1}$	–	$13.9^{+11.3}_{-11.2}$	–	–	3.69	0.47 (70)
Model 3	>200	$0.25^{+0.03}_{-0.03}$	$0.36^{+0.12}_{-0.13}$	–	–	2.12	0.85 (172)
	14.7[f]	$0.18^{+0.01}_{-0.01}$	$0.78^{+0.10}_{-0.10}$	–	–		1.135 (173)
Model 4	>49.3	–	<0.02	$12.7^{+12.5}_{-1.2}$	$35.6^{+10.0}_{-14.1}$	3.01	0.81 (172)
	14.7[f]	–	<0.06	$11.2^{+4.5}_{-3.4}$	$50.7^{+5.4}_{-5.1}$		0.85 (173)
Phase average							
Model 2[d]	$11.7^{+15.2}_{-4.4}$	–	$14.0^{+5.8}_{-4.2}$	–	–	4.29	0.49 (122)
Model 4	14.7[f]	–	<0.06	$9.79^{+1.69}_{-1.47}$	$56.9^{+2.1}_{-2.1}$	2.46	1.07 (275)

[a] Excluding the Fe K$_\alpha$ line band (6.0–7.2 keV). [b] Model 1/2 : single N_H, single kT. Model 3: single N_H, multi kT. Model 4: multi N_H, single kT. [c] The covering fraction (per cent) of N_{H1}. [d] Bolometric luminosity. The distance is assumed to be 100 pc. [e] Fitting in the 4.5–10.0 keV band. For other models, the 0.8–10.0 keV band is used. [f]Continuum temperature fixed at the value measured with *Ginga* (Ishida 1991).

consistent with the *Ginga* value. Considering that the K-edge absorption in the observed spectra is relatively shallow, the value of N_H obtained in this way is thought to approximate the covering fraction weighted mean value of multivalued absorption. The mean value of N_H in the accretion column is hence inferred to be $\sim10^{23}$ cm^{-2}.

Next we fitted the original 0.8–10.0 keV spectra (but excluding the iron K line region) by a two-temperature bremsstrahlung with single N_H, and obtained acceptable results (right-hand panel of Fig. 12 and Model 3 in Table 1). However, the first temperature kT_1 is still poorly determined; the fit became unacceptable for the pole-on spectra when we fixed kT_1 to the *Ginga* value. Furthermore, the obtained N_H is about 1×10^{22} cm^{-2} in either case, which is not consistent with the inference from the narrow band fitting. Thus, we regard Model 3 as inappropriate.

The fourth spectral model we employed consists of a single temperature bremsstrahlung and double-valued photoelectric absorption (N_{H1} and N_{H2}), which is the so-called partially covered absorption model (PCA model). This model is fully acceptable for both phases (Model 4 in Table 1). The obtained N_{H2} is consistent with that suggested by the narrow band fitting, and the fit remained good even when we fixed the temperature to the *Ginga* value. We therefore utilize this model (Model 4) as the best representation of the continua for both phases. The solid curves in Fig. 11 refer to this modelling.

4.3.2 *The Fe K lines*

Having quantified the continuum spectra of V834 Cen, we proceed to study the iron K line. For this purpose, we employ the phase-averaged spectrum, and again limit the energy range to the 4.5–10.0 keV band to avoid complex absorption structure in lower energies. As a first-cut attempt, we modelled the iron line with a single Gaussian model, while representing the continuum with a single-temperature bremsstrahlung absorbed with a single column density (to reproduce the iron K edge), but the fit failed to

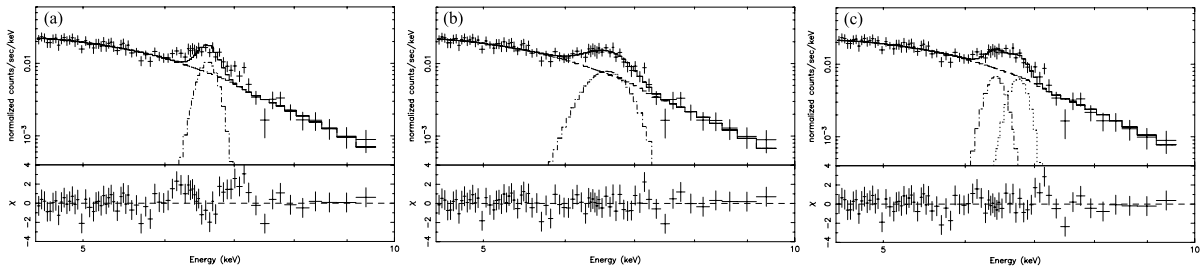

Figure 13. Phase-averaged SIS spectra in the iron K line energy band, fitted with a single narrow Gaussian (left-hand panel; (a), a single broad Gaussian (centre panel; (b), and a double narrow Gaussian model (right-hand panel; (c). The continuum spectrum is represented by a single temperature and a single column density in the 4.5–10.0 keV band (narrow band fitting). The best-fitting parameters are shown in Table 2.

Table 2. Best-fitting parameters of the iron K_α line[a].

Line model	Iron K_α line				Statistics
	L. C. 1[b] (keV)	σ_1 (keV)	L. C. 2[b] (keV)	σ_2 (keV)	χ^2_ν (dof)
Single narrow	$6.63^{+0.04}_{-0.05}$	0.0001[c]	–	–	1.37 (69)
Single broad	$6.66^{+0.05}_{-0.05}$	$0.29^{+0.06}_{-0.05}$	–	–	0.66 (68)
Double narrow	$6.45^{+0.08}_{-0.11}$	0.0001[c]	$6.79^{+0.23}_{-0.46}$	0.0001[c]	0.91 (67)

[a] The phase averaged spectrum. Only SIS data are used for the fitting. Fitted with a single temperature and single column density model in 4.5–10.0 keV. Fixed the continuum temperature and $N_{\rm H}$ to the Model 2 in Table 1. [b] Line centre energies. [c] Fixed.

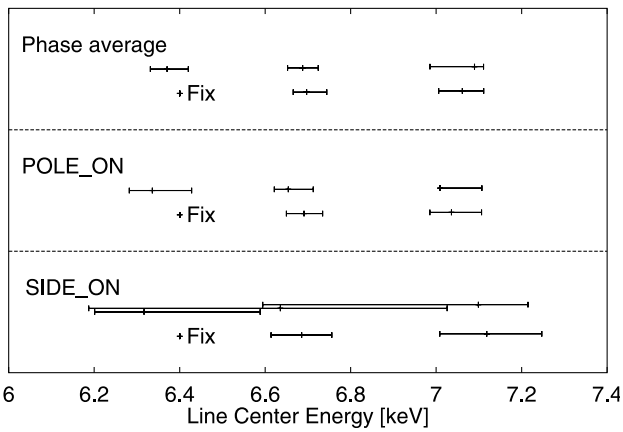

Figure 14. The best-fitting line centroid energies with 68 per cent errors in terms of the three narrow Gaussian model. From the top to bottom panels, the results for the phase average, pole-on phase, and side-on phase are shown. The upper plot in each panel shows the results when three centroid energies are left free. The lower plot shows the results when the centroid energy of the first Gaussian is fixed at 6.40 keV. The fit energy range is 4.5–10.0 keV.

reproduce the line profile, as shown in Fig. 13(a). A broad Gaussian model with $\sigma \sim 0.28$ keV has been found to be successful (Table 2; Fig. 13b), but the obtained line centroid energy is too low for ionized Fe K species which are expected for a plasma of temperature $\sim$10 keV. Alternatively, we can fit the data successfully with two narrow Gaussians (Table 2; Fig. 13c), where the centroid energy of the first Gaussian turned out to be consistent with that of the fluorescent iron K_α line (6.40 keV); that of the second Gaussian comes in-between those of the He-like iron K_α line (6.65–6.70 keV) and the H-like line (6.97 keV). This means that the second Gaussian is in reality a composite of the H-like and He-like lines.

We therefore employed a line model consisting of three narrow Gaussians, each having a free centroid energy and a free normalization. We then obtained an acceptable fit, with the three centroid energies consistent with the Fe K line energies of the neutral, He-like and hydrogen-like species, as shown in Fig. 14. These three lines have been observed in the spectra of many polars with *ASCA* (Ezuka & Ishida 1999). Hereafter, we adopt the 'three narrow Gaussians' model in quantifying the iron lines of V834 Cen.

As our final analysis, we have repeated the three-Gaussian fitting to the spectra, by fixing the line centroid energy of the first Gaussian (identified to a fluorescent line) at 6.40 keV. The result is of course successful, and the obtained parameters are given in Table 3 as well as Fig. 14. Fig. 15 shows the phase-resolved SIS spectra fitted with this model. To check consistency, we have expanded the energy range of the fit back to 0.7–10.0 keV, and performed full-band fitting, employing the continuum Model 4 and the three narrow Gaussians for the iron K line. The results, presented in Table 3, are generally consistent with those from the narrow-band analysis.

The temperature and $N_{\rm H}$ obtained in these final fits are thus the same between the two phases, within errors, and the EW of fluorescent and H-like lines are also consistent with being unmodulated. In contrast, the EW of the He-like line is enhanced by $(\xi_{\rm pole}/\xi_{\rm side})^{\rm obs} \equiv 1.87^{+0.54}_{-0.54}$ times (narrow band fitting) or $1.91^{+0.47}_{-0.64}$ times (full band fitting) in the pole-on phase compared to the side-on phase, with >90 per cent statistical significance.

5 DISCUSSION

5.1 Origin of the line intensity modulation in V834 Cen

In order to verify our interpretation, mentioned in Section 2, we observed the polar V834 Cen with *ASCA*. It has been confirmed that the EW of the He-like iron K_α line is enhanced by a factor of

Table 3. Best-fitting parameters of the iron K_α line with three narrow Gaussians.

Phase[a]	continuum		Fluorescent	He-like		H-like		χ^2_ν (dof)
	kT (keV)	N_H ($\times 10^{22}$ cm^{-2})	EW (eV)	l. c.[b] (keV)	EW (eV)	l. c.[b] (keV)	EW (eV)	
Narrow Band Fitting[c]								
Average	$9.3^{+10.4}_{-2.9}$	$15.4^{+5.9}_{-5.8}$	244^{+59}_{-83}	$6.70^{+0.06}_{-0.04}$	352^{+90}_{-91}	$7.07^{+0.08}_{-0.44}$	192^{+81}_{-97}	0.67 (154)
Pole-on	$9.6^{+20.3}_{-2.87}$	$15.6^{+8.0}_{-6.5}$	242^{+87}_{-102}	$6.69^{+0.07}_{-0.05}$	417^{+104}_{-113}	$7.04^{+0.11}_{-0.15}$	223^{+123}_{-118}	0.59 (140)
Side-on	$9.0^{+50.0}_{-1.0}$	$16.6^{+13.4}_{-9.5}$	270^{+122}_{-175}	$6.69^{+0.70}_{-0.13}$	223^{+94}_{-101}	$7.14^{+0.16}_{-0.48}$	223^{+123}_{-89}	0.64 (103)
Full Band Fitting[d]								
Average			347^{+53}_{-52}	$6.71^{+0.05}_{-0.06}$	456^{+57}_{-70}	$7.07^{+0.10}_{-0.08}$	230^{+88}_{-56}	1.05 (327)
Pole-on	(Model 4 in Table 1)[e]		229^{+164}_{-17}	$6.71^{+0.07}_{-0.10}$	650^{+19}_{-164}	$7.06^{+0.12}_{-0.15}$	282^{+58}_{-164}	0.98 (243)
Side-on			368^{+76}_{-119}	$6.71^{+0.62}_{-0.13}$	341^{+115}_{-111}	$7.13^{+0.21}_{-0.56}$	222^{+199}_{-105}	0.82 (210)

[a] Pole-on phase: $\phi = 0.73 \pm 0.25$. Side-on phase: $\phi = 0.23 \pm 0.25$. [b] The line centre (keV). That of the fluorescent component is fixed at 6.40 keV. [c] The determination of the continuum spectrum is performed in the 4.5–10.0 keV range with a single N_H and single temperature model. [d] The determination of continuum spectrum is performed in the 0.8–10.0 keV range with a multi N_H and single temperature model (Model 4 in Table 1). [e] The temperature is fixed to the *Ginga* value. Continuum parameters are fixed.

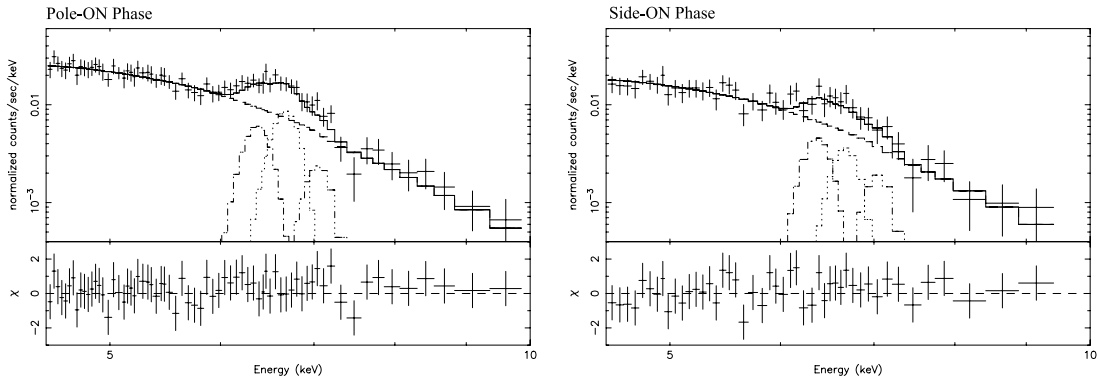

Figure 15. Phase-resolved spectra over the Fe K line energies, fitted with three narrow Gaussians. Left-hand panel: pole-on spectrum; right-hand panel: side-on spectrum. The central energy of the first Gaussian is fixed at 6.4 keV. The best-fitting parameters are shown in Table 3.

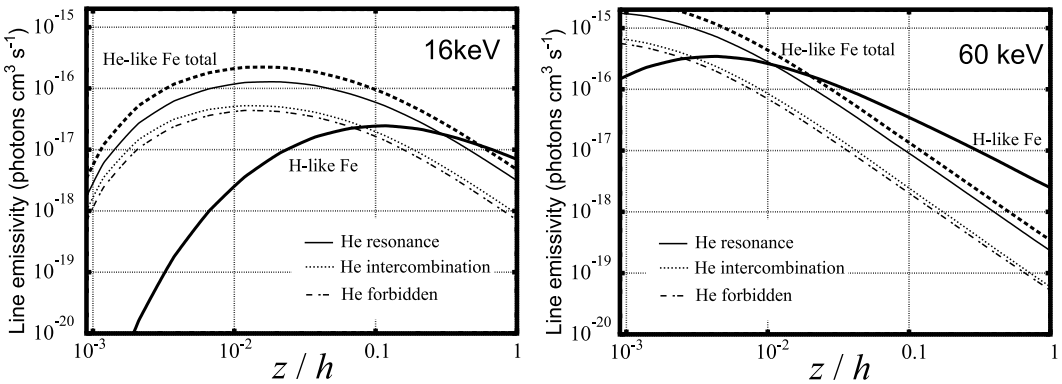

Figure 16. The volume emissivity of Fe K line photons in the assumed accretion column, shown as a function of z/h. The plasma temperature is $kT^{\rm sh} = 16$ keV (left-hand panel), and 60 keV (right-hand panel).

$(\xi_{\rm pole}/\xi_{\rm side})^{\rm obs} = 1.87 \pm 0.54$ in the pole-on phase relative to the side-on phase. Can we explain the observed rotational modulation of the He-like iron line EW of V834 Cen by some conventional mechanisms? An obvious possibility is that the temperature variation modulates the iron line intensity. However, the continuum temperature determined by the narrow band fitting (Table 3) is almost constant within errors, which explains the rotational modulation of the line intensity ratio. Alternatively, the bottom part of the accretion column, where the emissivity of the He-like iron line is highest (Fig. 16), may be eclipsed by the WD surface so that the He-like line is reduced in the side-on phase. However, such a condition does not occur under the geometrical parameters of V834 Cen. Furthermore, we do not see any dip in the rotation-folded, hard X-ray light curve. Therefore, this explanation is not likely either. A third possibility is that a part of iron line photons come from some regions other than the accretion column. In fact, X-rays

from polars are known to be contributed to by photons reflected from the WD surface (Beardmore et al. 1995; Done et al. 1995; Done & Magdziarz 1998). This mechanism can explain the production of fluorescent lines, and possibly the rotational modulation, but cannot produce highly ionized iron lines. From these considerations, we conclude that the observed iron line modulation is difficult to account for without appealing to resonance scattering effects.

Our next task is to examine whether the geometrical collimation mechanism (Section 2.1) can explain the observation. When the optical depth of resonance scattering is very high, and hence the line photons come solely from the surface of the accretion column, the angular distribution of the iron line intensity is given analytically by equation (B1) in Appendix B. By averaging this distribution under the geometry of V834 Cen, and taking into account the exposure for the two phases, we have calculated the expected line beaming factor ξ for the *ASCA* data as shown in Fig. 17. Thus, to explain the observed enhancement of He-like line solely by the geometrical beaming, a very flat coin-shaped column with $h/r \sim 0.2$ would be required. Furthermore, the observed ξ should be lower by about 30–40 per cent than the ideal calculation in Fig. 17, because finite optical depths, expected under a typical plasma density of polar accretion column, reduce the enhancement (Fig. 6). We hence conclude that the geometrical mechanism alone is insufficient to explain the observed He-like iron line enhancement in V834 Cen (Section 2), and hence the additional collimation caused by the velocity gradient effect is needed.

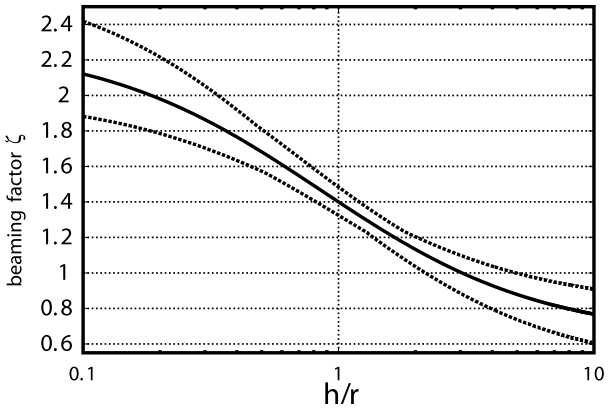

Figure 17. The expected line beaming factor $\xi_{\rm pole}/\xi_{\rm side}$ of V834 Cen caused by pure geometrical effects at the limit of large optical depth, calculated by considering the system geometry of V834 Cen and the exposure for each phase. It is shown as a function of h/r. The solid line corresponds to the most likely system geometry of $(i, \beta) = (45°, 25°)$, while the dashed lines reflect uncertainties in the system geometry.

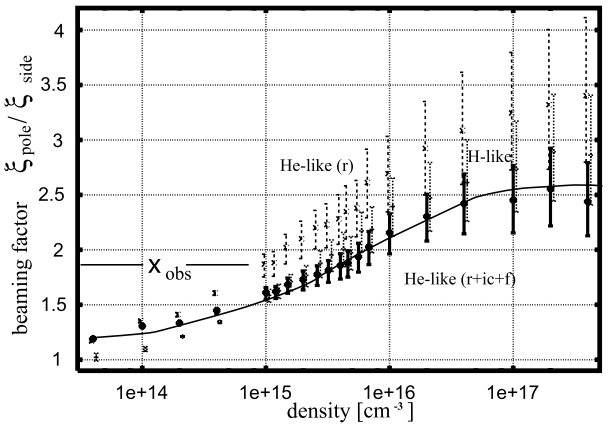

Figure 18. The expected beaming factor $\xi_{\rm pole}/\xi_{\rm side}$ of V834 Cen, as a function of the assumed post-shock density. It is calculated by Monte Carlo simulations under the actual observing condition with *ASCA*; i.e. the exposure in each phase is set to be the actual accumulation time with *ASCA*, and the viewing angle θ of each phase is calculated by the geometry of $i = 45°$, $\beta = 25°$. The shock temperature is set to 17.7 keV, and the volume emission measure is set to 1.30×10^{54} cm^{-3}. The dashed and dotted data points indicate ξ of He- and H-like resonance iron K_α photons, respectively. The solid data points show ξ of the blended He-like iron line, which includes intercombination and forbidden lines. The error bars take into account those of the geometrical parameters.

Are all the observed results consistently explained in our picture that incorporates the geometrical and velocity-gradient effects then? At the temperature of V834 Cen (~15 keV), the resonant photons in fact contribute about 65 per cent to the observed He-like iron K_α line, the rest coming from intercombination (~20 per cent) and forbidden (~15 per cent) lines which are free from the resonance scattering effects (Fig. 4). As a result, the line collimation is expected to be somewhat weakened in the *ASCA* spectra, where we cannot separate these unmodulated lines from the resonance line. After correcting for this reduction, the true value of ξ for the He-like resonance line is calculated to be ~2.3. This is within the range that can be explained by our scenario.

What about the H-like iron K_α line? Even though it consists entirely of resonant photons, its modulation in the V834 Cen data has been insignificant (Table 3). Presumably, this is mainly due to technical difficulties in detecting this weak line, under the presence of the stronger He-like line adjacent to it. Furthermore, we expect the hydrogen-like iron line to be intrinsically less collimated than the He-like resonance iron line, because the H-like line photons are produced predominantly in the top regions of the accretion column (Fig. 16): there, the electron density is lower, the thermal Doppler effect is stronger and the path of escape from the column is shorter, as compared to the bottom region where the He-like lines are mostly produced. Therefore, the H-like line is expected to be less collimated than the He-like resonance line (Fig. 18). Note that, with the energy resolution of *ASCA*, we cannot resolve the fine structure of He-like lines, so the collimation of the blended He-like line is expected to be almost comparable to that of the H-like line.

From these considerations, we conclude that the *ASCA* results on V834 Cen can be interpreted consistently by our POLE scenario.

5.2 Determination of the accretion column parameters

The line beaming effect we have discovered is expected to provide unique diagnostics of the accretion column of magnetic WDs. The physical condition in the accretion column is described by four parameters: $kT^{\rm sh}$, h, r and $n_e^{\rm sh}$. To determine these parameters, four observational or theoretical constraints are required. Usually, observations provide two independent quantities, the temperature $kT_{\rm OBS}$ and the volume emission measure (VEM), which is $\sim(n_e^{\rm sh})^2 hr^2$. Also there is one theoretical constraint, that the shock-heated plasma cools only by the free–free cooling, which relates $kT^{\rm sh}$, $n_e^{\rm sh}$, and h as in equation (A5).

With these three constraints, and taking into account Aizu's

Table 4. Geometrical parameters of randomly sampled polars, and values of ζ expected for them.

Object name	i [a]	β [b]	ζ [c]	Reference
BL Hyi	70 ± 10	153 ± 10	0.70	Cropper (1990)
UZ For	~ 88	~ 14	0.71	Ferrario et al. (1989)
VV Pup	76 ± 6	152 ± 6	0.71	Cropper (1990)
ST LMi	64 ± 5	141 ± 4	0.71	Cropper (1990)
AN UMa	65 ± 20	20 ± 5	0.87	Cropper (1990)
QQ Vul	65 ± 7	~ 23	0.88	Cropper (1990); Schwope et al. 2000; Catalan, Schwope & Smith (1999)
V1309 Ori	~ 80	~ 30	0.86	Harrop-Allin et al. (1997)
EF Eri	58 ± 12	27 ± 18	0.96	Cropper (1990)
AR UMa	50 ± 10	23 ± 13	1.05	Szkody et al. (1999)
WW Hor	~ 74	~ 48	1.06	Bailey et al. (1988)
DP Leo	76 ± 10	103 ± 5	1.06	Cropper (1990)
MR Ser	43 ± 5	38 ± 5	1.09	Cropper (1990)
J1015+0904	55 ± 5	43 ± 7	1.10	Burwitz et al. (1998)
V834 Cen	45 ± 9	25 ± 5	1.11	Cropper (1990)
AM Her	52 ± 5	66 ± 5	1.13	Wickramasinghe et al. (1991); Ishida et al. (1997)
EK UMa	56 ± 19	56 ± 19	1.14	Cropper (1990)
VY For	9 ± 3	~ 9	1.66	Beuermann et al. (1989)

[a] Inclination angle (°). [b] Pole colatitude (°). [c] Expected beaming factor to the average flux, assuming that the same collimation as the case of V834 Cen occurs and that only single accretion column emits.

solution (Aizu 1973), we can express h and r as

$$h = 1.61 \times 10^7 \,\mathrm{cm} \left(\frac{kT^{\mathrm{sh}}}{17.7\,\mathrm{keV}} \right)^{\frac{1}{2}} \left(\frac{n_e^{\mathrm{sh}}}{10^{16}\,\mathrm{cm}^{-3}} \right)^{-1} \tag{12}$$

$$r = 2.15 \times 10^7 \,\mathrm{cm} \left(\frac{\mathrm{VEM}}{1.30 \times 10^{54}\,\mathrm{cm}^{-3}} \right) \times \left(\frac{kT^{\mathrm{sh}}}{17.7\,\mathrm{keV}} \right)^{-\frac{1}{4}} \left(\frac{n_e^{\mathrm{sh}}}{10^{16}\,\mathrm{cm}^{-3}} \right)^{-\frac{1}{2}}. \tag{13}$$

Here, we normalized the VEM to the value of $1.30 \times 10^{54}\,\mathrm{cm}^{-3}$ obtained from V834 Cen, adopting a distance of 86 pc (Warner 1987). The value of $kT^{\mathrm{sh}} = 17.7$ keV was determined from the expected mass of WD by the observed ratio of H-like to He-like iron K_α lines, considering the vertical temperature gradient (fig. 5 of Ezuka & Ishida 1999); it is consistent with an independent calculation by Wu, Chanmugam & Shaviv (1995) based on the *Ginga* observation (Ishida 1991). When n_e^{sh} is low, the solutions to h and r imply a long, cylinder-like column, while a flat coin-shaped geometry is indicated by high values of n_e^{sh}. However, because of the lack of one more piece of information, the value of n_e^{sh} has so far been left undetermined. As a consequence, we have not been able to determine the column geometry.

The present work provides us with the needed fourth information, the value of ξ, which reflects the accretion column condition. Suppose we specify a value of n_e^{sh}. Then, equations (12) and (13) determine h and r respectively, which in turn are used as inputs to the Monte Carlo simulation to predict ξ. In this way, we have calculated ξ for V834 Cen as a function of n_e^{sh}, and show the results in Fig. 18. By comparing it with the observed value of $(\xi_{\mathrm{pole}}/\xi_{\mathrm{side}})^{\mathrm{obs}} \sim 1.87$, we obtain the best estimate as $n_e^{\mathrm{sh}} \sim 4.6 \times 10^{15}\,\mathrm{cm}^{-3}$. This in turn fixes the column height as $h \sim 3.5 \times 10^7$ cm and the radius as $r \sim 3.2 \times 10^7$ cm. These values are considered to be typical for polars.

Currently, the errors on $\xi_{\mathrm{pole}}/\xi_{\mathrm{side}}$ are so large that the value of n_e^{sh} is uncertain by almost an order of magnitude, with the allowed range being 1×10^{14}–$1 \times 10^{16}\,\mathrm{cm}^{-3}$. However, our new method will provide a powerful tool for next generation instruments with a larger effective area and an improved energy resolution.

5.3 Effects on the abundance estimates

The iron abundance of other polars, measured by Ezuka & Ishida (1999), are subject to some changes when we properly consider the resonance scattering effects. For this purpose, we show in Table 4 the geometrical parameters (i and β) of 17 polars, which have been randomly selected from ~50 currently known polars. The expected enhancement $\zeta \equiv \sum_{\mathrm{phase}} \xi$ are also listed with the assumption that the resonance lines are collimated as much as those in the case of V834 Cen. Thus, the implied corrections to the iron abundances of these objects are at most ±30 per cent, which is generally within the measurement error. Polars with almost side-on or almost pole-on geometry, such as POLEs, are subject to a relatively large modification in the abundance estimates, but such a geometry is a rare case (here, only VY For). Therefore, the distribution of metal abundances of polars, 0.1–0.8 solar, measured by Ezuka & Ishida (1999) is still considered valid.

5.4 Mystery of POLEs

Our Monte Carlo simulation (Section 3) and the observed study of V834 Cen (Section 4) consistently indicate that the resonance iron K lines are enhanced by a factor of $\xi_{\mathrm{m}} = 2$–2.5 in the axial direction of accretion column. The effect is thought to be ubiquitous among polars, because we have so far employed very typical conditions among them. Consequently, if a polar with co-aligned magnetic axis ($\beta \sim 0$) is viewed from behind the pole-on direction ($i \sim 0$), we expect the iron K line EW to be persistently enhanced by 2–2.5 times. When this enhancement is not considered, such objects would yield artificially higher metallicity by similar factors. We conclude that the three POLEs (Section 1) are exactly such objects.

In condition of $\zeta > 2$, the extremely high face-value abundances of AX J2315−0592 will be modified to be ~1 solar, and

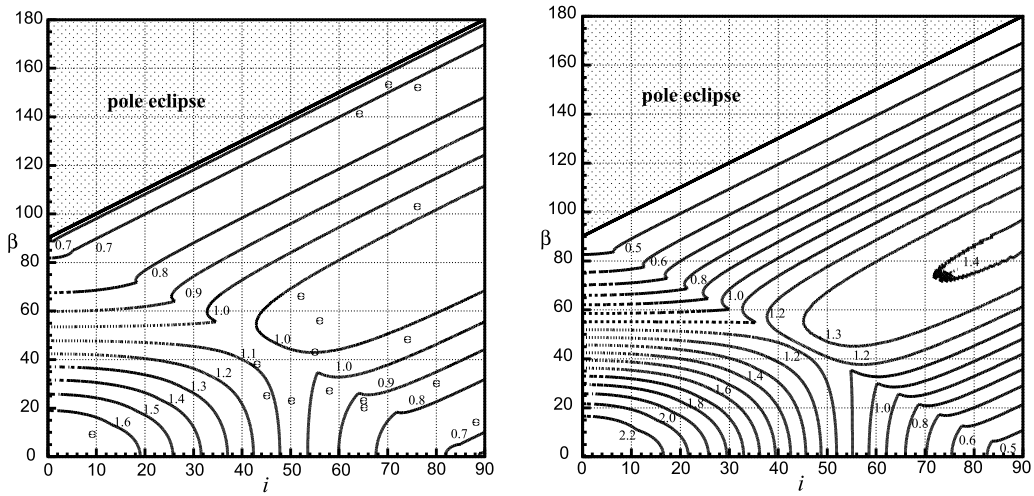

Figure 19. The expected enhancement ζ to the average line intensity calculated on the plane of (i, β), assuming that accretion column exists only on one pole with the same collimation as the case of V834 Cen (left-hand panel) or the strong case shown in text (right-hand panel). Contour levels are shown in the figure. The polars listed in Table 4 are also plotted in the left-hand panel with dots.

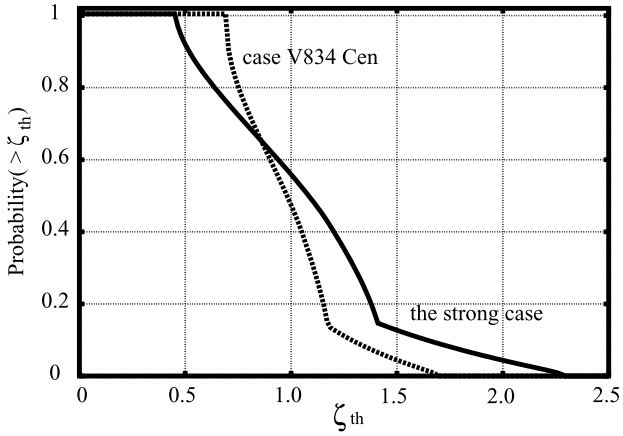

Figure 20. The cumulative probability distribution of finding ζ higher than the specified threshold $\zeta_{\rm th}$, assuming that objects are randomly distributed in terms of i and β. The dotted and solid curves represent the case of V834 Cen and the strong case, respectively.

abundance of RX J1802.1+1804 or AX J1842−0423 comes into the measured distribution of other polars within errors. We can expect a strong collimation with an adequate density of $n_{\rm e} \sim 10^{16}\,{\rm cm}^{-3}$ (Fig. 8b) and an adequate shape of $h/r \sim 0.1$–0.5 (Fig. 8a) with typical radius $\sim 10^7$ cm. Thus, one example of strong collimation calculated for He-like iron resonance line is in the condition that temperature of 10 keV, $r = 5 \times 10^7$ cm, $n_{\rm e} = 7.9 \times 10^{15}\,{\rm cm}^{-3}$ and VEM $= 10^{55}\,{\rm cm}^{-3}$, which yield an X-ray luminosity of $1.0 \times 10^{32}\,{\rm erg\,s}^{-1}$ (2–10 keV). Hereafter, we call this condition the strong case. Fig. 19 shows the expected enhancement ζ of iron He-like line (sum of resonance line, intercombination line and forbidden line) with various geometrical conditions (i and β). In Fig. 20, we have converted the result of Fig. 19 into cumulative probability distribution of ζ. We hence expect $\zeta > 2$ at the condition of strong case shown above, with a probability of ∼4.5 per cent. This estimate is in rough agreement with the observation, i.e. the three POLEs among the ∼50 known polars. We reconfirm that the iron abundances derived from the observation (Ezuka & Ishida 1999) remains valid to within 30 per cent for a major fraction of polars. Thus, we conclude that the mystery of POLEs have been solved by the proposed line-collimation mechanism.

6 CONCLUSION

In order to explain the extremely intense iron K lines observed from several Galactic X-ray sources (including two polars; Section 1), we have developed a scenario of POLEs, that the iron lines from accretion poles of magnetic WDs are axially collimated by the two mechanisms (Section 2) which become operational under large optical depths for the resonant line scattering. One mechanism is the geometrical effect, which becomes effective when the accretion column is rather short, while the other is a physical mechanism where the Doppler shifts caused by the vertical velocity gradient in the post-shock flow reduces the cross-section for resonance scattering along the field lines.

In Section 3, we have carried out Monte Carlo simulations, and confirmed that the velocity-gradient effect, augmented by the geometrical effect, can enhance the iron K line EW in the pole-on direction by a factor of up to 3.0 as compared to the angular average. This is higher than the maximum collimation available with the geometrical effect alone (Appendix B).

In order to verify our interpretation experimentally, we have analysed the *ASCA* data of V834 Cen, which has a suitable geometry in that our line-of-sight to the accretion column changes from 20° to 70° as the WD rotates, in Section 4. Through detailed phase-resolved X-ray spectroscopy, it has been confirmed that the EW of the He-like iron-K$_\alpha$ line is enhanced by a factor of $(\xi_{\rm pole}/\xi_{\rm side})^{\rm obs} = 1.87 \pm 0.54$. In Section 5.1, we have examined whether the observation can be explained away by any other mechanism, and we have concluded that this observational result of V834 Cen strongly reinforces our interpretation of POLEs.

Although the resonance lines are collimated with the proposed beaming effect, the previous measurements of the distribution of metal abundances of polars is considered still valid (Section 5.3) except for POLEs. With the proposed mechanism, the extremely high face-value abundances observed in POLEs can be reconciled with the average abundance measured from the other polars. Thus, the POLE scenario successfully solves the mystery of the extremely strong iron lines observed from the three X-ray sources.

In addition, our scenario provides a new method of the unique determination of physical conditions in the accretion column, using the beaming factor of resonance lines as a new source of observational information (Section 5.2). This will be a powerful method for the next generation instruments.

ACKNOWLEDGMENTS

We thank the members of the *ASCA* team for spacecraft operation and data acquisition.

REFERENCES

Aizu K., 1973, Prog. Theor. Phys., 49, 1184
Bailey J., Axon D. J., Hough J. H., Watts D. J., Giles A. B., Greenhill J. G., 1983, MNRAS, 205, 1
Bailey J., Wickramasinghe D. T., Hough J. H., Cropper M., 1988, MNRAS, 234, 19
Beardmore A. P., Ramsay G., Osborne J. P., Mason K. O., Nousek J. A., Baluta C., 1995, MNRAS, 273, 742
Beuermann K., Thomas H.-C., Giommi P., Tagliaferri G., Schwope A. D., 1989, A&A, 219, 7
Burke B. E., Mountain R. W., Daniels P. J., Cooper M. J., Dolat V. S., 1994, IEEE Trans. Nucl. Sci., NS-41, 375
Burwitz V. et al., 1998, A&A, 331, 262
Catalán M. S., Schwope A. D., Smith R. C., 1999, MNRAS, 310, 123
Cropper M., 1990, SSRv, 54, 195
Done C., Osborne J. P., Beardmore A. P., 1995, MNRAS, 276, 483
Done C., Osborne J. P., 1997, MNRAS, 288, 649
Done C., Magdziarz P., 1998, MNRAS, 298, 737
Ezuka H., Ishida M., 1999, ApJS, 120, 277
Ferrario L., Wickramasinghe D. T., Bailey J., Tuohy I. R., Hough J. H., 1989, ApJ, 337, 832
Fujimoto R., Ishida M., 1997, ApJ, 474, 774
Greiner J., Remillard R. A., Motch C., 1998, A&A, 336, 191
Harrop-Allin M. K., Cropper M., Potter S. B., Dhillon V. S., Howell S. B., 1997, MNRAS, 288, 1033
Hoshi R., 1973, Prog. Theor. Phys., 49, 776
Ishida M., 1991, PhD thesis, Univ. Tokyo
Ishida M., Matsuzaki K., Fujimoto R., Mukai K., Osborne J. P., 1997, MNRAS, 287, 651
Ishida M., Greiner J., Remillard R. A., Motch C., 1998, A&A, 336, 200
Makishima K. et al., 1996, PASJ, 48, 171
Mewe R., Gronenschild E. H. B. M., van den Oord G. H. J., 1985, A&AS, 62, 197
Misaki K., Terashima Y., Kamata Y., Ishida M., Kunieda H., Tawara Y., 1996, ApJ, 470, 53
Norton A. J., Watson M. G., 1989, MNRAS, 237, 853
Ohashi T. et al., 1996, PASJ, 48, 157O
Rybicki G. B., Lightman A. P., 1979, Radiative Processes in Astrophysics. Wiley, New York
Schwope A. D., Thomas H.-., Beuermann K., Reinsch K., 1993, A&A, 267, 103
Schwope A. D., Catalán M. S., Beuermann K., Metzner A., Smith R. C., Steeghs D., 2000, MNRAS, 313, 533
Serlemitsos P. J. et al., 1995, PASJ, 47, 105
Spitzer L., 1962, Physics of Fully Ionized Gases. Wiley, New York
Szkody P., Vennes S., Schmidt G. D., Wagner R. M., Fried R., Shafter A. W., Fierce E., 1999, ApJ, 520, 841
Terada Y., Kaneda H., Makishima K., Ishida M., Matsuzaki K., Nagase F., Kotani T., 1999, PASJ, 51, 39 (Paper I)
Thomas H.-C., Reinsch K., 1996, A&A, 315, L1
Warner B., 1987, MNRAS, 227, 23
Wickramasinghe D. T., Bailey J., Meggitt S. M. A., Ferrario L., Hough J., Tuohy I. R., 1991, MNRAS, 251, 28
Wu K., Chanmugam G., Shaviv G., 1995, ApJ, 455, 260
Yamashita A. et al., 1997, IEEE Trans. Nucl. Sci., NS-44

APPENDIX A: PLASMA IN AN ACCRETION COLUMN OF A WHITE DWARF

A flow of accreting matter captured by the magnetic field of WD channels into an accretion column, where a standing shock forms and heats up the matter to a temperature $kT^{\rm sh}$ of

$$kT^{\rm sh} = \frac{3}{8}\frac{GM_{\rm WD}\mu m_{\rm H}}{R_{\rm WD}} = 16\left(\frac{\mu}{0.615}\right)\left(\frac{M_{\rm WD}}{0.5\,{\rm M}_\odot}\right)\left(\frac{R_{\rm WD}}{10^9\,{\rm cm}}\right)^{-1}\ {\rm keV}, \quad \text{(A1)}$$

where k is the Boltzmann constant, G is the gravitational constant, $M_{\rm WD}$ is the WD mass (typically $0.5\,{\rm M}_\odot$), and $R_{\rm WD}$ is the radius of the WD (typically 10^9 cm). Thus the plasma has a typical temperature of hard X-ray emitter, forming an accretion column as illustrated in Fig. 1. The velocity beneath the shock front $u^{\rm sh}$ is described with a relation to the free-fall velocity $u_{\rm ff}$ of

$$u^{\rm sh} = \frac{u_{\rm ff}}{4} = \frac{1}{4}\sqrt{\frac{2GM_{\rm WD}}{R_{\rm WD}}} = 0.9\times10^8\left(\frac{M_{\rm WD}}{0.5\,{\rm M}_\odot}\right)^{1/2}\left(\frac{R_{\rm WD}}{10^9\,{\rm cm}}\right)^{-1/2}\ {\rm cm\,s^{-1}}. \quad \text{(A2)}$$

Assuming that the plasma is a single fluid and that the abundance is one solar, the electron density of the post-shock plasma is given as

$$n_e^{\rm sh} \simeq \left(\frac{\dot{M}}{\pi r^2 u^{\rm sh}\mu m_{\rm H}}\right)\times 0.518 = 7.7\times10^{15}\left(\frac{\dot{M}}{10^{16}\,{\rm g\,s^{-1}}}\right) \times\left(\frac{M_{\rm WD}}{0.5\,{\rm M}_\odot}\right)^{-1/2}\left(\frac{R_{\rm WD}}{10^9\,{\rm cm}}\right)^{1/2}\left(\frac{r}{5\times10^7\,{\rm cm}}\right)^{-2}\ {\rm cm^{-3}}, \quad \text{(A3)}$$

where the value 0.518 is the fraction of electron density to the total density, assuming solar abundance. In the accretion column, kT, u and n_e all have a vertical gradient from the shock front toward the WD surface. Numerically, the vertical profiles of these quantities as a function of the distance z from the WD surface, normalized by h, are calculated by Aizu (1973) as

$$\frac{kT}{kT^{\rm sh}} = \frac{u}{u^{\rm sh}} = \left(\frac{n_e}{n_e^{\rm sh}}\right)^{-1} \simeq \left(\frac{z}{h}\right)^{\frac{2}{5}}, \quad \text{(A4)}$$

where each quantity is normalized to its value immediately below the shock front; $kT^{\rm sh}$, $u^{\rm sh}$ and $n_e^{\rm sh}$.

The column radius of the accretion column is typically $r = 5\times10^7$ cm. Because the shock front is sustained by the pressure of the post-shock plasma against the gravity, h is described by the free–free cooling time-scale $t_{\rm ff_{cool}}$ of the heated plasma as $h \sim u^{\rm sh} t_{\rm ff_{cool}}$. According to Aizu (1973), h is given more specifically as

$$h = 0.605 u^{\rm sh} t_{\rm ff_{cool}} = 1.9\times10^7\left(\frac{kT^{\rm sh}}{16\,{\rm keV}}\right)^{\frac{1}{2}}\left(\frac{n_e^{\rm sh}}{7.7\times10^{15}\,{\rm cm^{-3}}}\right)^{-1}\ {\rm cm}, \quad \text{(A5)}$$

where $t_{\rm ff_{cool}}$ is given by

$$t_{\rm ff_{cool}} \equiv \frac{3n_e kT^{\rm sh}}{2\epsilon_{\rm ff}} = 0.35\left(\frac{kT^{\rm sh}}{16\,{\rm keV}}\right)^{\frac{1}{2}}\left(\frac{n_e^{\rm sh}}{7.7\times10^{15}\,{\rm cm^{-3}}}\right)^{-1}\ {\rm s}, \quad \text{(A6)}$$

with $\epsilon_{\rm ff}$ as the volume emissivity of free–free emission (eqution 5.15 in Rybicki & Lightman 1979). Note that the ion-to-electron energy transfer time-scale $t_{\rm eq}$ is

$$t_{\rm eq} = 5.6\times10^{-3}\left(\frac{kT^{\rm sh}}{16\,{\rm keV}}\right)^{\frac{3}{2}}\left(\frac{n_e^{\rm sh}}{7.7\times10^{15}\,{\rm cm^{-3}}}\right)^{-1}{\rm s} \quad \text{(A7)}$$

(see equation 5.31 in Spitzer 1962) is much shorter than $t_{\rm ff_{cool}}$, so the ions and electrons are thought to share the same temperature.

At the temperature of a few tens of keV (equation A1), the electron scattering dominates the opacity in the hard X-ray band. Actually, the optical depth of the accretion column for free–free absorption, $\tau_{\rm ff}$, is given, relative to the electron scattering optical depth $\tau_{\rm T}$ (equation 1) as

$$\tau_{\rm ff} = 0.88 \times10^{-10}\tau_{\rm T}\left(\frac{E}{6\,{\rm keV}}\right)^{-2}\left(\frac{kT}{16\,{\rm keV}}\right)^{-\frac{3}{2}}\left(\frac{n_e^{\rm sh}}{7.7\times10^{15}\,{\rm cm^{-3}}}\right) \quad \text{(A8)}$$

(see equation 5.18 in Rybicki & Lightman 1979). Thus, the free–free absorption is negligible compared to Thomson scattering.

The cross-section of resonance scattering $\sigma_{\rm RS}$ for a photon with energy E_0 can be described generally as

$$\sigma_{\rm RS} = \frac{\pi e^2}{m_{\rm i}c}f_{12}\frac{1}{\sqrt{2\pi}\Delta E}\exp\left\{-\frac{(E_0-E_{\rm RS})^2}{2\Delta E^2}\right\}{\rm cm^{-3}} \quad \text{(A9)}$$

where f_{12} is the oscillator strength for Lyα transition ($n=1$ to 2), $E_{\rm RS}$ is the resonance energy in the rest frame, and ΔE is a resonance energy width (equation 10.70 in Rybicki & Lightman 1979). Numerically, the first factor is $\pi e^2/m_{\rm Fe}cf_{12} = 1.2\times10^{-17}\,{\rm cm^{-3}}$, and the energy width ΔE in the second factor of Gaussian is determined by equations (5) and (6). Then, the cross-section of resonance scattering at the line-centre energy is given as

$$\sigma_{\rm RS} = 2.0\times10^{-18}\left(\frac{E_0}{6.695\,{\rm keV}}\right)\left(\frac{kT}{16\,{\rm keV}}\right)^{-1/2}{\rm cm^2}. \quad \text{(A10)}$$

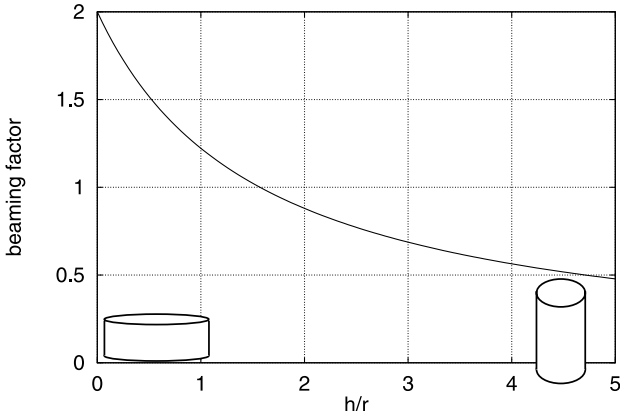

Figure 21. The beaming factor of a pure geometrical beaming using equation (B2). The absolute value of the vertical axis shows the ratio of the flux from pole-on ($\theta=0$) viewing and the averaged flux with angle θ.

APPENDIX B: GEOMETRICAL BEAMING IN THE ACCRETION COLUMN

How much enhancement can we expect in 'geometrical beaming' in the accretion column (see Section 2.1)? Consider the case where the resonance line photons can only escape from the surface of the column. The directional photon flux emerging from the column is given as

$$f(\theta)\,{\rm d}\cos\theta \propto \pi r^2\cos\theta + 2rh\sin\theta, \quad \text{(B1)}$$

where θ is the angle measured from the column axis. Therefore, the flux along $\theta\simeq0$ is enhanced by a factor

$$\frac{f(\theta)}{\langle f\rangle} = \frac{\pi r^2}{(1/2)\pi r^2 + (\pi/2)rh} = \frac{2}{1+(2/\pi)(h/r)}, \quad \text{(B2)}$$

where $\langle f\rangle$ is the average of $f(\theta)$ over θ. At the coin-shaped limit [$(h/r)\rightarrow0$], this factor approaches 2 (Fig. 21).

This paper has been typeset from a TEX/LATEX file prepared by the author.